Neuron
NeuroResource

Cell PRESS

High-Resolution Proteomics Unravel Architecture and Molecular Diversity of Native AMPA Receptor Complexes

Jochen Schwenk,[1,4,5] Nadine Harmel,[3,5] Aline Brechet,[1] Gerd Zolles,[1] Henrike Berkefeld,[1] Catrin Swantje Müller,[1] Wolfgang Bildl,[1] David Baehrens,[1] Björn Hüber,[1] Akos Kulik,[1,4] Nikolaj Klöcker,[3] Uwe Schulte,[1,2,4,*] and Bernd Fakler[1,4,*]

[1]Institute of Physiology, University of Freiburg, Hermann-Herder-Str. 7, 79104 Freiburg, Germany
[2]Logopharm GmbH, Hermann-Herder-Str. 7, 79104 Freiburg, Germany
[3]Institute of Neuro- and Sensory Physiology, University of Düsseldorf Medical Faculty, 40225 Düsseldorf, Germany
[4]Centre for Biological Signaling Studies (BIOSS), Albertstr. 10, 79104 Freiburg, Germany
[5]These authors contributed equally to this work
*Correspondence: uwe.schulte@physiologie.uni-freiburg.de (U.S.), bernd.fakler@physiologie.uni-freiburg.de (B.F.)
DOI 10.1016/j.neuron.2012.03.034

SUMMARY

AMPA-type glutamate receptors (AMPARs) are responsible for a variety of processes in the mammalian brain including fast excitatory neurotransmission, postsynaptic plasticity, or synapse development. Here, with comprehensive and quantitative proteomic analyses, we demonstrate that native AMPARs are macromolecular complexes with a large molecular diversity. This diversity results from coassembly of the known AMPAR subunits, pore-forming GluA and three types of auxiliary proteins, with 21 additional constituents, mostly secreted proteins or transmembrane proteins of different classes. Their integration at distinct abundance and stability establishes the heteromultimeric architecture of native AMPAR complexes: a defined core with a variable periphery resulting in an apparent molecular mass between 0.6 and 1 MDa. The additional constituents change the gating properties of AMPARs and provide links to the protein dynamics fundamental for the complex role of AMPARs in formation and operation of glutamatergic synapses.

INTRODUCTION

Fast excitatory neurotransmission in the mammalian brain largely relies on AMPA receptors (AMPARs) that control fundamental aspects of development and signal transduction in glutamatergic synapses. During the early phase of synaptogenesis, AMPARs are recruited to dendritic sites of contact with axons where they promote both formation and maturation of synapses (McAllister, 2007; McKinney, 2010). In established synapses, AMPARs mediate the fast excitatory postsynaptic current (EPSC) that initiates propagation of the electrical signal and controls Ca^{2+} entry into the postsynaptic spine (Cull-Candy et al., 2006; Garaschuk et al., 1996; Jonas and Spruston, 1994; Raman and Trussell, 1992; Sah et al., 1990; Silver et al., 1992).

The time course and the amplitude of the AMPAR-mediated EPSCs are quite variable among neurons and strongly depend upon the gating properties of the receptor channels (Conti and Weinberg, 1999; Jonas, 2000). The number of AMPARs in the postsynaptic membrane is determined by trafficking and endo/exocytic processes (Bredt and Nicoll, 2003; Carroll et al., 2001; Choquet, 2010; Choquet and Triller, 2003; Shepherd and Huganir, 2007). All of these processes appear to be regulated via posttranslational modifications and protein interactions and together are thought to endow excitatory synaptic transmission with the activity-dependent plasticity underlying learning, memory, and/or maintenance of synapses (Derkach et al., 2007; Malenka and Nicoll, 1999; Malinow and Malenka, 2002; Newpher and Ehlers, 2008).

On the molecular level, the complexity in the cell biology of AMPARs is met by a number of distinct protein constituents: native AMPARs are assembled from the pore-forming GluA1-4 proteins (Collingridge et al., 2009; Hollmann and Heinemann, 1994; Seeburg, 1993) and at least three types of auxiliary subunits, the transmembrane AMPAR regulatory proteins (TARPs γ-2, γ-3, γ-4, γ-5, γ-7, γ-8; Cho et al., 2007; Milstein et al., 2007; Soto et al., 2009; Tomita et al., 2003), the *cornichon* homologs (CNIH-2, CNIH-3; Schwenk et al., 2009), and the CKAMP44 protein (von Engelhardt et al., 2010). Alone or in combination, these auxiliary subunits control the gating and pharmacology of the AMPARs and profoundly impact their biogenesis and protein processing (Bats et al., 2007; Chen et al., 2000; Gill et al., 2011; Harmel et al., 2012; Kato et al., 2010; Schober et al., 2011; Schwenk et al., 2009; Soto et al., 2007; Tomita et al., 2005; Vandenberghe et al., 2005; von Engelhardt et al., 2010).

It is not clear, however, whether these auxiliary proteins represent the whole set of building blocks for native AMPARs or whether they contain additional yet unknown protein constituents. Likewise, quantitative data on the subunit composition of native AMPAR complexes are not yet available. This information may be obtained from comprehensive and quantitative proteomic analyses as have recently been presented for the Cav2 family of voltage-gated calcium channels (Müller et al., 2010).

Here we used two orthogonal biochemical strategies, multiepitope and target knockout-controlled affinity purifications (Bildl et al., 2012; Müller et al., 2010) and newly developed high-resolution quantitative analyses of protein complexes separated on native gels (BN-MS), for investigation of the subunit composition of AMPARs from total brain. These analyses unravel native AMPARs as macromolecular complexes of unanticipated complexity and identify 21 novel protein constituents, mostly transmembrane or secreted proteins of low molecular mass and with distinct functions. Subsequent studies using antibody shift assays, binding studies, and electrophysiological recordings reveal the architecture of native AMPARs and demonstrate that properties and function of the receptor complexes may be quite distinct strongly depending on the particular subunit composition.

RESULTS

Multiepitope Proteomic Analysis of AMPAR Complexes in the Brain

For comprehensive proteomic analysis of native AMPARs, we performed multiepitope affinity purifications (ME-APs) (Müller et al., 2010; Schwenk et al., 2010) with ten different antibodies (ABs) specific for the GluA1-4 proteins on membrane fractions prepared from total brains of adult rats, wild-type (WT) mice, and AB-target knockout mice (see Experimental Procedures). For ME-APs the membrane fractions were treated with detergent buffers of either mild (CL-47) or intermediate (CL-91) stringency (Müller et al., 2010; Schwenk et al., 2010) solubilizing ~40% and 100% of the total pool of AMPARs, respectively (Figures S1A and S1B). These buffers were selected as the two extremes in a test series probing the solubilization efficiency of various CL-buffers as well as of RIPA and Triton X-100, the buffers most widely used with AMPARs (Kim et al., 2010; Shi et al., 2009, 2010; Vandenberghe et al., 2005; solubilization efficiency of ~60%, Figure S1B). Both CL-47 and CL-91 preserved high-molecular-weight AMPAR complexes (Schwenk et al., 2009) as demonstrated by blue native polyacrylamide gel electrophoresis (BN-PAGE); the AMPAR complexes focused over an apparent molecular mass range of ~0.4 MDa under either condition, although they appeared slightly smaller in CL-91 than in CL-47 (Figure 1A). Total eluates of APs with the anti-GluA ABs or with pools of preimmunization immunoglobulins G (IgG) were analyzed by high-resolution nanoflow liquid chromatography tandem mass spectrometry (nano-LC MS/MS), which provided data on both the identity and the amount of proteins. Protein amounts were determined from the peak volumes (PVs) of their best-correlating tryptic peptides (TopCorr method [Bildl et al., 2012]; see also Experimental Procedures), a label-free quantification method offering a linear dynamic range of up to four orders of magnitude (Bildl et al., 2012; Müller et al., 2010; Schwenk et al., 2010).

The results of these MS analyses showed that AMPARs were retained in all APs with high efficiency as reflected by the PV values and the extensive coverage provided for the primary sequence of the GluA1-4 proteins by the MS/MS-identified peptides (relative sequence coverage of 90%, 95%, 95%, 83% for GluA1 to GluA4, respectively; Tables S1–S3; detailed information on all aspects related to MS analyses were deposited at http://www.channel-proteomes.com/projects). The other

proteins identified by mass spectrometry in the anti-GluA APs (and surpassing the threshold PV, see Experimental Procedures) were evaluated for both their specificity and consistency of copurification with the GluA proteins based on the quantitative data of protein amounts. Specificity of copurification was determined from abundance ratio plots using both target knockouts and preimmunization IgGs as negative controls (upper-right quadrant in Figure 1B; Table S3; Bildl et al., 2012; Müller et al., 2010). Consistency was assessed by the number of specific copurifications of a given protein across the anti-GluA APs; a protein was considered consistent if it was specifically retained in at least five (out of ten) or three (out of five) anti-GluA APs using solubilization with CL-91 and CL-47, respectively.

Together, the criteria abundance threshold, specificity, consistency, and confirmation by at least one of the knockout controls defined a sharp-profiled proteome (Figure 1C), identifying 34 (out of 1,711 detected) proteins as high-confidence constituents of native AMPARs in the rodent brain (Table 1). As summarized in Figure 1D, these constituents comprise the aforementioned AMPAR subunits GluA1-4, five members of the TARP family (γ-5 was unambiguously detected in only three out of 15 APs, albeit in small amounts), CNIHs 2,3, and CKAMP44 as well as another 22 proteins of which only DLG4 (or PSD95) has been previously described as an AMPAR interactor (Chen et al., 2000). Similar to the known auxiliary subunits, the majority of the newly identified AMPAR constituents are low-molecular-weight proteins (between 15.3 and 55.4 kDa; Figure 1D) and most of them were copurified effectively under both solubilization conditions resulting in a marked relative coverage of their primary sequences (between 25% and 100%, Figure 1D). Interestingly, 12 of these new constituents (out of 21) are transmembrane (TM) proteins of different classes (1–8 TM domains), while five are secreted and four are cytoplasmic proteins (Table 1). Robust association of these proteins with native AMPARs was corroborated in reverse APs where ABs targeting a selected set of known and newly identified AMPAR constituents replaced the anti-GluA ABs. As shown in Figure S1C, all of the ABs effectively retained the GluA proteins together with many of the other AMPAR proteome constituents.

Quantification of Subunit Composition by BN-Mass Spectrometry

While ME-APs are suited to reliably identify constituents of protein assemblies, they may not entirely reflect their native abundances and stoichiometries, mainly due to the inherent properties of ABs (Müller et al., 2010; Schulte et al., 2011). We therefore used an AB-free BN-MS approach (Remmerie et al., 2011; Wessels et al., 2009) exploiting the sharp focusing of AMPAR complexes in the BN-PAGE (Figure 1A). Sections of native gel regions harboring the AMPARs (from total brain of adult rats) were sliced with a cryotome (thickness of slices 400 μm) and collected, and each slice was analyzed individually for its protein composition by quantitative MS-analysis (Figure 2A; see Experimental Procedures). Together with calibration peptides specific for the identified AMPAR constituents (Figure 1D) and concatenated into fusion proteins at defined stoichiometry (QconCAT proteins; Pratt et al., 2006; Figure S2A, Table S4), this procedure allowed for quantitative assessment of the molecular composition of AMPAR
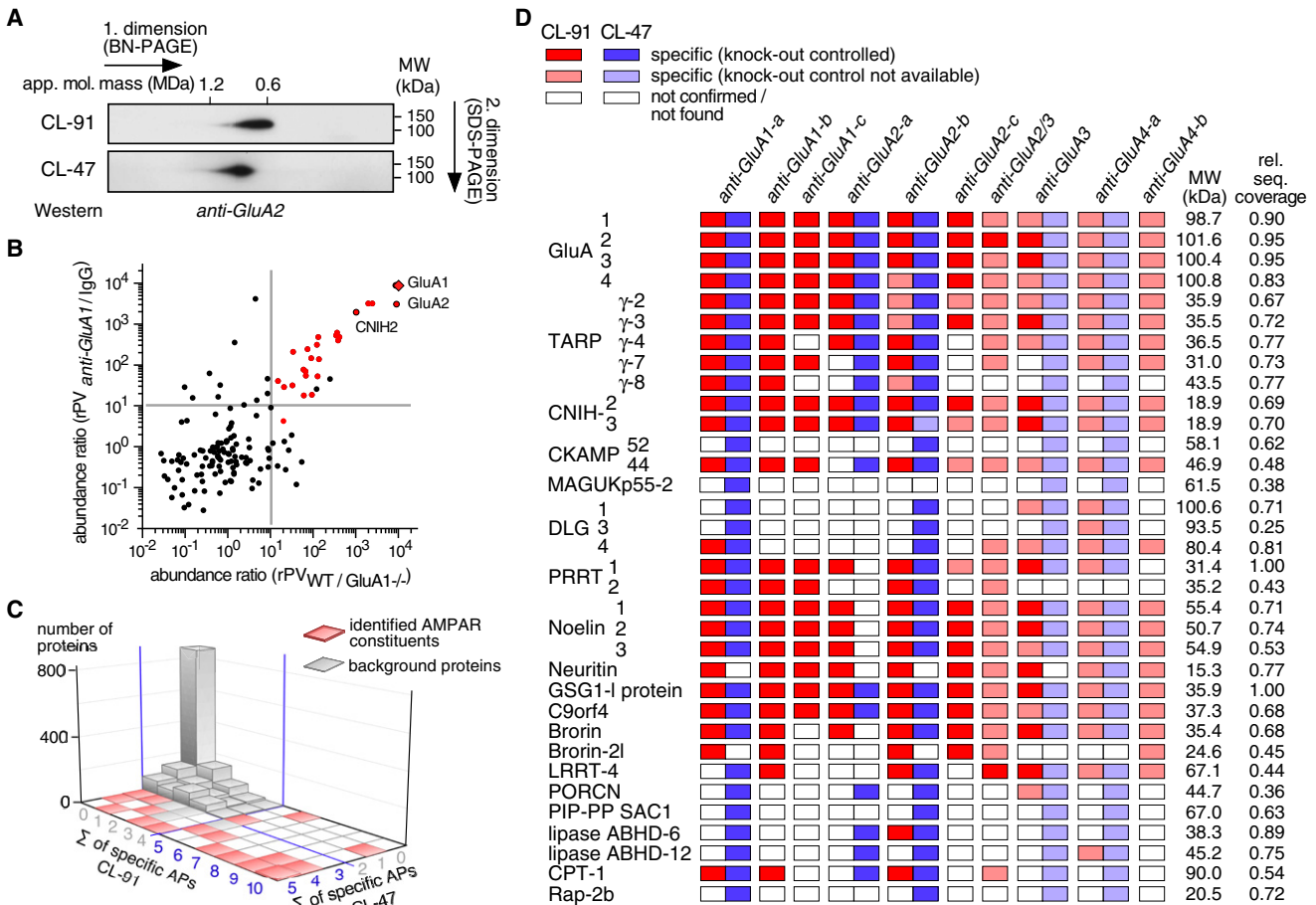
Figure 1. ME-AP Proteomics Identify the Protein Constituents of Native AMPARs

(A) Two-dimensional gel separation of AMPAR complexes from rat brain solubilized with CL-91 and CL-47; both gel separations were western-probed with the indicated antibody. Size (BN-PAGE) and molecular weight (SDS-PAGE) are as indicated.

(B) Two-dimensional logarithmic abundance-ratio plot illustrating the medians of PV ratios (rPV) obtained for any protein in APs from rat membranes with the *anti-GluA1-a* AB versus IgG (y axis) and in *anti-GluA1-a* APs from mouse membranes of WT versus GluA1 knockout animals (x axis). Gray bars (rPVs of 10) represent the specificity threshold for this AB on either rPV scale and place specifically purified proteins in the upper-right quadrant. Red dots denote finally annotated AMPAR constituents (D, Table 1); black dots symbolize all other proteins. Red dot in the lower-right and black dots in the upper-right quadrant represent peculiarities of the *anti-GluA1-a* AP.

(C) Three-dimensional plot illustrating the consistency of specifically copurified proteins detected in the *anti-GluA* APs performed with CL-91 (10 APs) and CL-47 (5 APs). Blue lines indicate the consistency thresholds given in the text, and numbers are the count of APs that specifically copurified a given protein. Red bars refer to the counts of finally annotated AMPAR constituents, and gray bars denote counts of background proteins; the four proteins surpassing the consistency threshold of CL-47 failed confirmation by knockout controls. Note the sharp discrimination between AMPAR constituents and background.

(D) Table summarizing the results for all of the finally annotated AMPAR constituents across the 15 APs performed with the indicated *anti-GluA* ABs. Color coding given in the upper left; MW and relative coverage of the primary sequence as indicated on the right.

complexes of a given apparent molecular mass (Figure 2A; see Experimental Procedures).

Figure 2B shows the resulting abundance profiles obtained from 81 consecutive gel slices for the most ample constituents of AMPARs solubilized with CL-47. Thus, the major portion of AMPAR complexes exhibited an apparent molecular mass of about 0.6–1.0 MDa, markedly exceeding the size of the GluA tetramers (mass of ∼0.5 MDa, Figure S2C). For the pore-forming subunits, BN-MS revealed an abundance sequence of GluA2 > GluA1 > GluA3 > GluA4, with the molecular amount of GluA2 being equal to the sum of the other GluAs (Figure 2B, upper panel). Among the known auxiliary subunits, TARP γ-8 and CNIH-2 were by far the most abundant (Figures 2B and 2E). Comparison of the abundance value determined for all TARP and CNIH proteins with that obtained for the entire pool of AMPARs (defined as GluA tetramers, GluA$_{tetra}$) yielded a ratio of about 4:1 (Figure 2C), strongly suggesting that, on average, AMPAR complexes contain up to four TARP or CNIH proteins in line with previous reports on heterologously expressed AMPARs (Kim et al., 2010; Shi et al., 2009).

Moreover, the BN-MS approach revealed cosegregation of the newly identified AMPAR constituents with the GluA proteins,

Table 1. Protein Constituents of Native AMPARs as Identified by ME-APs

Protein ID	Name	Alternative Name(s)	Acc. No. (SwissProt)
GluA1	AMPA-type glutamate receptor 1	GluR-A	P19490
GluA2	AMPA-type glutamate receptor 2	GluR-B	P19491
GluA3	AMPA-type glutamate receptor 3	GluR-C	P19492
GluA4	AMPA-type glutamate receptor 4	GluR-D	P19493
TARP γ-2	Transmembrane AMPA-regulatory protein γ-2	Stargazin	O88602
TARP γ-3	TARP γ-3		Q8VHX0
TARP γ-4	TARP γ-4		Q8VHW9
TARP γ-7	TARP γ-7		P62957
TARP γ-8	TARP γ-8		Q8VHW5
CNIH-2	protein *cornichon* homolog 2		Q5BJU5
CNIH-3	protein *cornichon* homolog 3		Q6ZWS4
CKAMP44	Cystine-knot AMPAR modulating protein of 44 kDa	Protein shisa-9	Q9CZN4
CKAMP52	Cystine-knot AMPAR modulating protein of 52 kDa	Protein shisa-6	Q3UH99
MAGUKp55-2	MAGUK p55 subfamily member 2	Protein MPP2	Q9WV34
DLG1	Disks large homolog 1	SAP-97	Q62696
DLG3	Disks large homolog 3	SAP-102	Q62936
DLG4	Disks large homolog 4	PSD-95, SAP-90	Q62108
PRRT1	Proline-rich transmembrane protein 1	NG-5, SynDIG4	Q6MG82
PRRT2	Proline-rich transmembrane protein 2		Q7Z6L0
Noelin1	Noelin-1	Olfactomedin-1, Pancortin	Q62609
Noelin2	Noelin-2	Olfactomedin-2	Q8BM13
Noelin3	Noelin-3	Olfactomedin-3	P63057
Neuritin	Neuritin	CPG-15	O08957
GSG1-l protein	Germ cell-specific gene 1-like protein		Q6UXU4
C9orf4	Uncharacterized protein C9orf4	brain protein CG-6	Q9P0K9
Brorin	Brorin, von Willebrand factor C domain-containing protein 2	brain-specific chordin-like protein	Q8C8N3
Brorin-2l	von Willebrand factor C domain-containing protein 2-like		Q505H4
LRRT4	Leucine-rich repeat transmembrane neuronal protein 4		Q80XG9
PORCN	Probable protein-cysteine N-palmitoyltransferase porcupine	Porc, Ppn	Q9JJJ7
PIP-PP SAC1	Phosphatidylinositide phosphatase SAC1		Q9EP69
lipase ABHD-6	Monoacylglycerol lipase ABHD6		Q8R2Y0
lipase ABHD-12	Monoacylglycerol lipase ABHD12		Q99LR1
CPT-1	Carnitine O-palmitoyltransferase 1 (brain isoform)	CPT-1C	Q8BGD5
Rap-2b	Ras-related protein Rap-2b		P61227

☐ transmembrane   ☐ secreted   ☐ cytoplasmic

Accession numbers refer to the UniProt/SwissProt database; protein classification is given by the color-coding at the bottom.
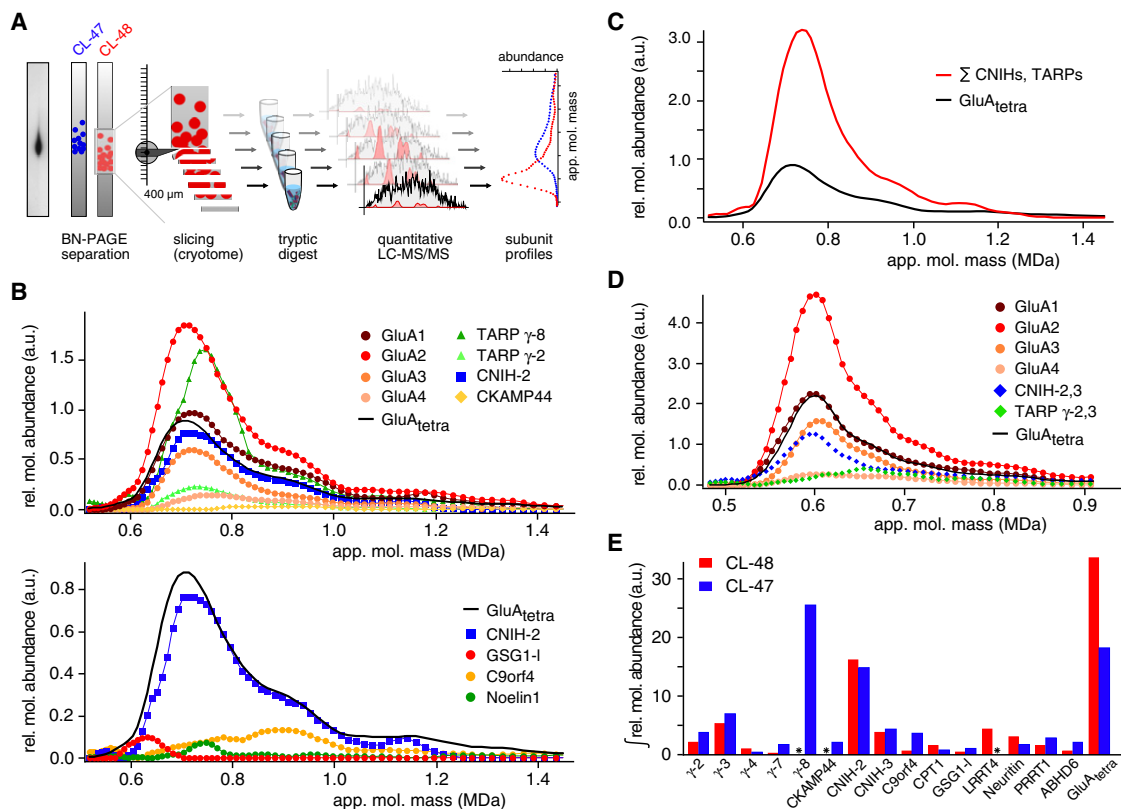
Figure 2. BN-MS Quantifies Subunit Composition of Native AMPAR Complexes of Given Molecular Mass

(A) Scheme illustrating the BN-MS approach used for high-resolution analysis of the subunit composition of native AMPARs (details in the text and Experimental Procedures).

(B and C) Abundance-mass profiles determined for AMPAR complexes solubilized with CL-47. Each data point represents the amount determined for the respective protein in one gel slice (total of 81 gel slices); symbols are as indicated. GluA$_{tetra}$ (black line) refers to the summed amounts of GluA1-4 divided by 4, and the red line in (C) is the sum of protein amounts determined for CNIHs 2,3 and TARPs γ-2,3,4,7,8. Note the distinct profiles obtained for GSG1-l, C9orf4 and Noelin-1.

(D) Abundance-mass profiles as in (C) but determined for AMPAR complexes solubilized with CL-48 (total of 69 gel slices).

(E) Bar graph illustrating total relative molecular abundance (integral over the investigated mass range) of the indicated AMPAR constituents determined in buffers CL-48 (red) and CL-47 (blue); asterisks denote missing data.

thus providing independent evidence for their robust association with native AMPAR complexes (Figure 2B, lower panel). As indicated by the abundance-mass profiles, these proteins either assemble into distinct AMPAR complexes of defined molecular mass (such as GSG1-l or Noelin1, Figure 2B, lower panel) or may be integrated into multiple types of complexes extending over a broader mass range (such as C9orf4 or CKAMP44, Figure 2B, upper and lower panel). The abundance values of all newly identified proteins were below those of TARP γ-8 and CNIH-2, but well in the range of the other TARPs, CNIH-3, or CKAMP44 (Figures 2B and 2E).

Subsequent BN-MS analysis of AMPAR complexes solubilized with buffers of intermediate stringency (CL-48, CL-91) revealed three further important features. First, the difference in the observed molecular size of AMPARs (Figure 1A), corresponding to ~0.1 MDa, is predominantly due to the almost complete dissociation of TARP γ-8 from the AMPARs under these conditions (Figures 2D and 2E); this quantitative dissociation was confirmed in density gradient centrifugations (Fig-

ure S2B) but was only seen with TARP γ-8, while the other TARPs remained largely unaffected (Figures 2D and 2E; Figure S2B). Second, some of the newly identified constituents including LRRT4 and Neuritin were more abundantly detected with the intermediate stringency buffers (Figure 2E). Third, the abundance profiles of CNIHs 2,3 and TARPs γ-2,3 indicate that they are predominantly assembled into distinct AMPAR complexes at an approximate ratio of 3:1 (Figure 2D), in line with our previous work (Schwenk et al., 2009).

Together, the results from ME-APs and BN-MS indicated that native AMPARs are in fact formed by a multitude of protein complexes assembled from up to 34 proteins at distinct abundance.

Multiple Populations of AMPAR Complexes with Distinct Stability

The assembly of native AMPARs was further investigated in AB-shift assays separating complexes in BN-PAGE by the additional mass of target-specific ABs and in APs probing the stability of
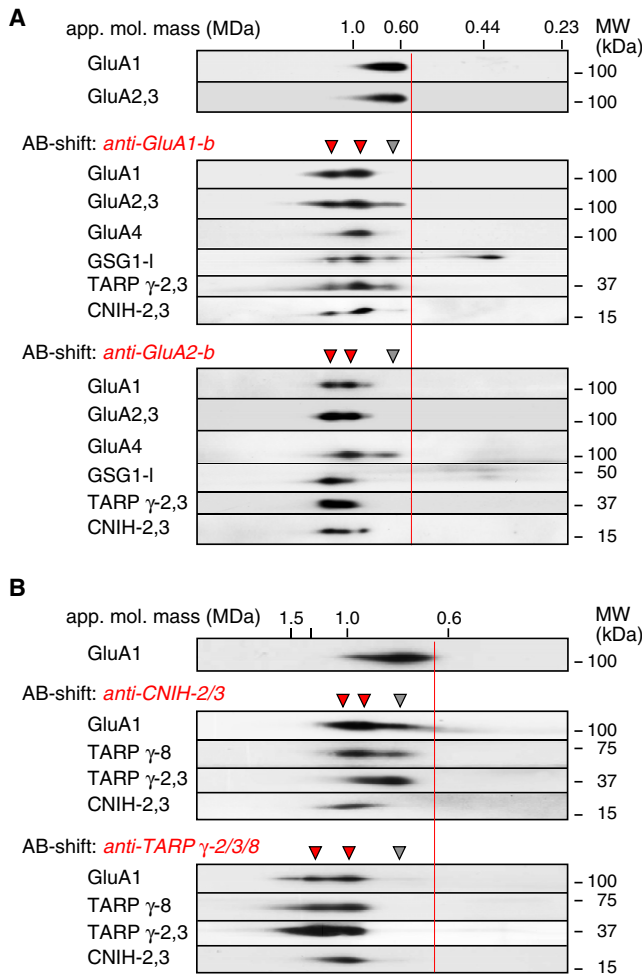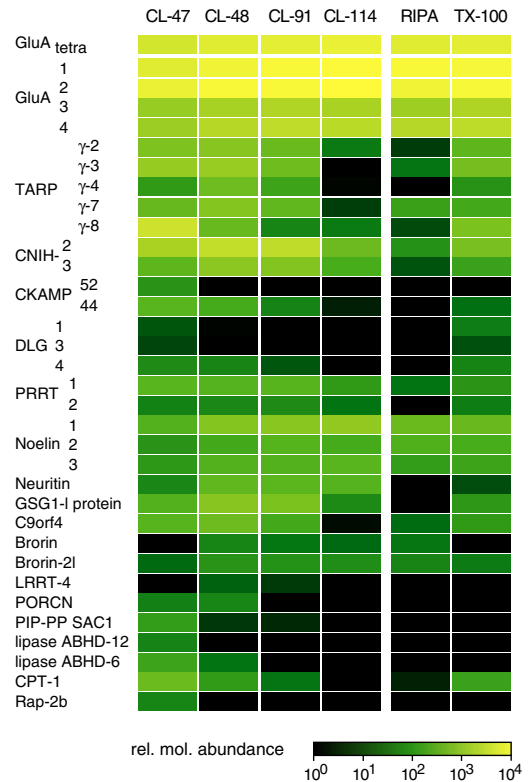
Figure 3. AMPAR Constituents Cosegregate into Multiple Populations of AMPAR Complexes

(A) Two-dimensional gel separation of AMPARs as in Figure 1 without (upper panel) and with ABs specific for either GluA1 (*anti-GluA1-b*) or GluA2 (*anti-GluA2-b*; lower two panels, AB-shift assay) added to the membrane fractions solubilized with CL-91; all gel separations were western-probed with ABs against the indicated proteins. Arrowheads denote unshifted (gray) or populations of AMPARs shifted by addition of one or two ABs (red).

(B) AB-shift assay as in (A) but with ABs targeting either CNIHs 2,3 or TARPs γ-2,3,8 and membrane fractions solubilized with CL-47.


Figure 4. AMPAR Constituents Coassemble into AMPAR Complexes with Distinct Stability

Heat map indicating the molecular abundance of all AMPAR constituents determined in *anti-GluA1-a* APs from membrane fractions solubilized with the indicated buffers. Stringency of solubilization buffers increased from CL-47 to CL-114 (Müller et al., 2010); results obtained with two widely used buffers, Triton X-100 and RIPA, were added for comparison.

complexes by an array of solubilization buffers with different stringency.

ABs specific for GluA1 and GluA2 shifted the majority of all GluAs to higher molecular weights (Figure 3A), with the discrete increments most likely reflecting assembly of at least one or two of these subunits into the respective AMPARs (also Figure S3); additionally, both assays revealed a small fraction of AMPARs devoid of either GluA1 or GluA1-3. The known auxiliary subunits TARP γ-2,3 and CNIH-2,3 were coshifted with both *anti-GluAs*, very similar to the GSG1-l protein, as expected for tightly associated complex constituents (Figure 3A). Interestingly, *anti-GluA2*, different from *anti-GluA1*, shifted the complete pool of GSG1-l, strongly suggesting preferred association of this newly identified

subunit with GluA2-containing AMPARs (Figure 3A). Shift assays with *anti-CNIH-2/3* showed that the majority of AMPARs solubilized at CL-47 (Figure S3B) are associated with the CNIHs (also Figure 2D), as well as with TARP γ-8, while most of the TARP γ-2,3 proteins are assembled into distinct subpopulations of AMPARs (Figure 3B, upper panel). Moreover, an AB targeting TARPs γ-2,3,8 indicated that virtually all AMPARs solubilized under these conditions contained at least one of the three TARP isoforms; AB-shift assays with both *anti-TARPγ-2/3/8* and *anti-CNIH-2/3* showed that these auxiliary subunits assemble into all native AMPARs and that the obtained mass shift (Figure S3C) is in line with the 4:1 ratio determined for GluA tetramers and TARPs plus CNIHs (Figure 2C). Notably, the two shift assays in Figure 3B (separated on the same gel) point toward distinct stoichiometries of these auxiliary subunits in native AMPARs, up to two CNIHs and two or more TARPs γ-2,3,8 per complex.

The stability of the AMPAR assemblies was assessed by determining the molecular abundance (using the QconCAT proteins as in Figure 2) of its constituents retained in *anti-GluA1-a* APs under solubilization conditions of increasing stringency (Müller et al., 2010) (see Experimental Procedures). Analysis of the resulting heat map (Figure 4) suggested that the
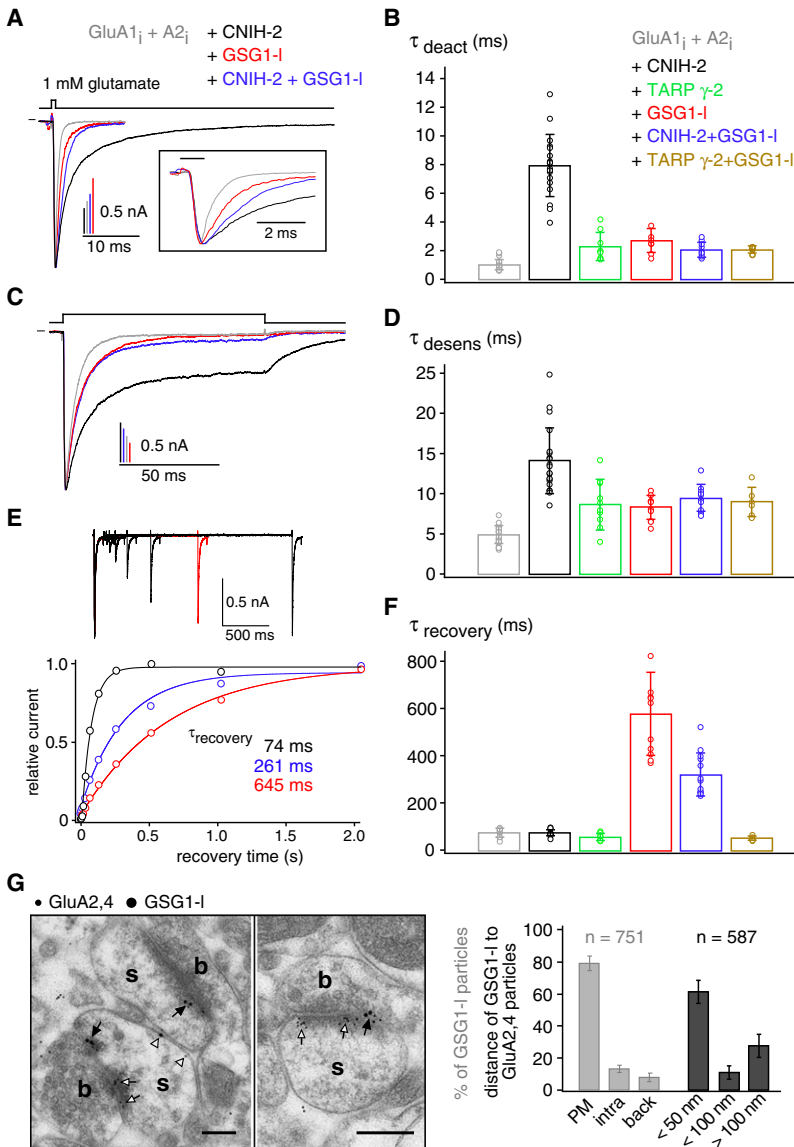
Figure 5. The GSG1-l Protein Assembles into Synaptic AMPARs and Modifies the Gating Kinetics of Receptor Channels in a Subunit-Dependent Manner

(A) Representative current responses of AMPARs recorded upon 1 ms (A) and 100 ms (C) applications of 1 mM glutamate (indicated above the current trace) in giant outside-out patches excised from *Xenopus* oocytes expressing GluA1$_i$ and GluA2$_i$ either alone (gray trace) or in combination with either CNIH-2 (black trace), GSG1-l (red trace) or both (blue trace). cRNAs of GluA1$_i$ and GluA2$_i$, CNIH-2, and GSG1-l were injected at equal amounts. Inset: current responses at expanded time scale; agonist application indicated by the horizontal bar.

(B and D) Bar graphs summarizing the time constants for deactivation and desensitization (mean ± SD of 6–19 experiments, represented by dots).

(E) Recovery of the same AMPARs as in (A) and (C) from steady-state desensitization recorded with a double-pulse protocol (pair of a 100 ms and a 50 ms glutamate pulse separated by increasing time intervals). Data points are peak currents recorded during the second pulse and normalized to the maximal current (recorded during the first glutamate application). Lines are monoexponential fits to the data points with the indicated $\tau_{recovery}$. Inset: Original current recordings from GluA1$_i$+A2$_i$+GSG1-l receptors; red trace is response with a recovery interval of 1024 ms.

(F) Bar graph summarizing the recovery time constants (mean ± SD of 6–15 experiments, represented by dots).

(G) Immunoelectron micrographs for GluA2,4 and GSG1-l in the CA3 region of the adult mouse hippocampus detected by postembedding immuno-EM (left panel) and respective statistics (right panel). Immunoparticles for GluA2 and GluA4 (10 nm, open arrows) and GSG1-l (15 nm, filled arrows) were mostly found over asymmetrical synapses between boutons (b) and dendritic spines (s) of pyramidal cells and were sparsely detected at extrasynaptic sites (arrowheads). Note that most immunoparticles for GSG1-l were detected in close spatial relationship (<100 nm) with those for GluA2 and GluA4. Scale bars are 0.2 mm; bars on the right are mean ± SD of three independent experiments. PM, intra, and back denote localization of immunoparticles to the plasma membrane, intracellular sites, and background, respectively.

underlying protein interactions may be classified into three main categories: interactions (1) that are largely unaffected by both intermediate (CL-48, CL-91) and high-stringency conditions (CL-114; as for CNIHs, Noelins, Neuritin, or PRRTs), (2) that are markedly reduced under conditions of high stringency (as for TARPs γ-2,3,4,7, GSG1-l, C9orf4, CKAMP44, DLG4, or PORCN), and (3) interactions mainly preserved at low-stringency conditions (CL-47; as for TARP γ-8, SAC1, DLG1,3, or CKAMP52). It is noteworthy that the stability of individual interactions was independent of their topology and in most cases not dependent upon the presence of the abundant auxiliary subunits. Thus, CNIH-2,3 and other tightly associated constituents were extensively retained in APs using conditions that did not preserve assembly of TARP γ-8 (Figure 4), or where the TARP γ-8 protein was absent after gene knockout (Figure S4). In addition, the heat map demonstrated that solubilization with

RIPA and Triton X-100 buffers failed to preserve integrity of all AMPAR complexes, resulting in the loss of a number of constituents (including LRRT4, Neuritin, Brorin, Brorin-2l, CKAMP52, and PORCN) readily detected in mild and/or intermediate stringency CL-buffers (Figure 4).

Functional Diversity by Heteromultimerization of Complex Constituents

The robust integration into defined AMPAR complexes together with CNIHs and TARPs (Figures 2B, 3, and 4), prompted us to investigate the functional significance of the GSG1-l protein for which no primary function has yet been described. Figures 5A and 5C show representative current responses recorded in giant outside-out patches from *Xenopus* oocytes upon 1 ms and 100 ms applications of 1 mM glutamate to AMPARs assembled either from the flip variants of GluA1 and GluA2 alone or in

combination with the additional constituents GSG1-l or CNIH-2 or both. Channel activation was similar in all four types of receptors (20%–80% rise times of ∼0.3 ms), but the time courses of deactivation (Figure 5A) and desensitization (Figure 5C) were markedly different, strongly depending upon the subunit composition of the AMPARs. While GSG1-l alone caused a moderate slowing of both kinds of channel closure very similar to TARP γ-2 ($p < 0.001$, Wilcoxon rank test for ± GSG1-l; Figures 5B and 5D), it largely reversed the pronounced effects of CNIH-2 on the time constants of deactivation and desensitization when coassembled into the same AMPARs ($p < 0.001$, Wilcoxon rank test for CNIH-2 versus CNIH-2+GSG1-l; Figures 5B and 5D). Moreover, receptor channels assembled from GluA1, GluA2, CNIH-2, and GSG1-l no longer exhibited the marked non-desensitizing steady-state current (I_{ss}) observed with receptors composed of the GluA1, GluA2, and CNIH subunits alone (I_{ss} of 25% ± 10% [mean ± SD, n = 20] and 6% ± 3% [n = 12] for GluA1+A2+CNIH-2 and GluA1+A2+CNIH-2+GSG1-l channels, respectively). In contrast to the moderate slowing of desensitization, GSG1-l decelerated the reverse process, recovery from desensitization, by almost 10-fold, and a pronounced slowing was still present upon addition of CNIH-2, albeit to a lesser extent ($p < 0.001$, Wilcoxon rank test for ± GSG1-l and ± GSG1-l+CNIH-2; Figures 5E and 5F). Interestingly, the dominant effects of GSG1-l over CNIH-2 in AMPAR gating were not recapitulated in receptors where CNIH-2 was replaced by TARP γ-2 ($p > 0.7$, Wilcoxon rank test for TARP γ-2 versus TARP γ-2+GSG1-l; Figures 5B, 5D, and 5F). Conversely, the CNIH-2 effects on gating were only moderately affected by coassembly of the TARP γ-8 subunit(s) ($p > 0.7$ and $p < 0.001$ Wilcoxon rank test for τ_{desens} and $\tau_{recovery}$, respectively; Figure S5A).

Together, these results demonstrated that coassembly of various auxiliary subunits generates AMPARs with quite distinct functional properties. The particular effects of GSG1-l may modulate the gating of AMPARs in various regions of the brain including the hippocampal CA3 region, where postembedding immunogold electron microscopy colocalized this protein with GluA2- and/or GluA4-containing AMPARs in dendritic spines of pyramidal cells (Figures 5G and S5B).

Subunit Composition and Architecture of Native AMPARs

Next, we used comparison of protein amounts obtained in *anti-GluA* APs from WT and GluA1 or GluA2 knockout mice and quantitative data from BN-PAGE separations (as in Figures 2 and 3, see Experimental Procedures) to probe whether the identified AMPAR constituents are preferentially associated with one of the two most abundant GluA subunits. Figure 6A summarizes the respective results together with the topology of the complex constituents suggested by public databases. Accordingly, very few of the AMPAR constituents are preferentially associated with either GluA1 (PRRT1,2) or GluA2 (GSG1-l, LRRT4, Brorin, and Brorin-2l). Twelve proteins (out of 30) appeared to exclusively associate with AMPARs (over other complexes in membrane fractions from adult brain) including the TARPs, CKAMP44, C9orf4, LRRT4, GSG1-l, and the two CNIH proteins whose complete pool was copurified with *anti-GluAs* (Figure S6A).

Finally, we combined the proteomic, biochemical and functional data (Figures 1–5) with Pearson correlation analyses across all data sets (Figure S6B) and binding assays on heterologously coexpressed complex constituents (Figure S6C) to derive a general (working) model for the assembly of native AMPARs in the brain. Accordingly, the model projected onto the recently resolved crystal structure of the GluA tetramer (Sobolevsky et al., 2009) reflects binding sites, their potential occupancies, and/or direct interactions of complex constituents, while exact stoichiometries of individual AMPARs or structural details are not implicated. As illustrated in Figure 6B, AMPARs share a common "inner core" that is assembled from four GluAs and four major auxiliary subunits (Figure 2C) arranged in a two-fold symmetry determined by the structure of the GluA tetramer just above the membrane plane (gray line in Figure 6A; Sobolevsky et al., 2009). Of the two pairs of distinct binding sites (solid circles in red and gray, Figure 6B), one is occupied either by CNIHs 2,3 (70%–80%, Figures 2 and 3) or TARPs γ-2,3 (20%–30%, Figures 2 and 3), the other harbors TARPs γ-8,4,2,3 or GSG1-l (Figures 2, 3, and 5). This inner core of the AMPARs is complemented by "outer core" constituents binding directly to the GluA proteins (Figure S6C) at sites distinct from the interaction sites of the inner core constituents (dashed circles in orange, Figure 6B): the one TM-domain proteins PRRTs 1,2, CKAMP44, or C9orf4, as well as the membrane-anchored Neuritin. As an entity, the proteins of the inner and outer core serve as a platform for other, more peripherally associated AMPAR constituents including the Noelins, Brorin-2l, and CPT-1 (Figure 6B); the latter were found tightly correlated with Neuritin and C9orf4, respectively (Figure S6B).

Together, the arrangement of a common inner core and variable extensions toward the periphery promotes formation of AMPARs with the range in size and variability in molecular composition unraveled by our proteomic analyses (Figures 1–4).

DISCUSSION

We showed that native AMPARs in the adult mammalian brain are multiprotein assemblies with unanticipated complexity. Coassembly of the known subunits with the 21 newly identified constituents into core and periphery of the receptor channels generates AMPARs with diverse properties and reflects the complex cell physiology of this main excitatory neurotransmitter receptor.

The Subunit Assembly of Native AMPARs

For thorough analysis of the building blocks of native AMPARs we used two complementary approaches, the ME-AP procedure (Figure 1) for identification of the protein constituents and an advanced BN-MS technique (Figure 2) for determination of their relative molecular abundance and quantitative analysis of the subunit assembly. Comprehensiveness and specificity of the identified AMPAR proteome were ensured by several key features of the ME-AP approach: (1) the use of multiple ABs compensating for the pitfalls intrinsic to individual ABs (Müller et al., 2010; Schulte et al., 2011), (2) sensitivity and dynamic range of our nano-LC MS/MS analysis extending over three to four orders of magnitude (Bildl et al., 2012; Müller et al., 2010),
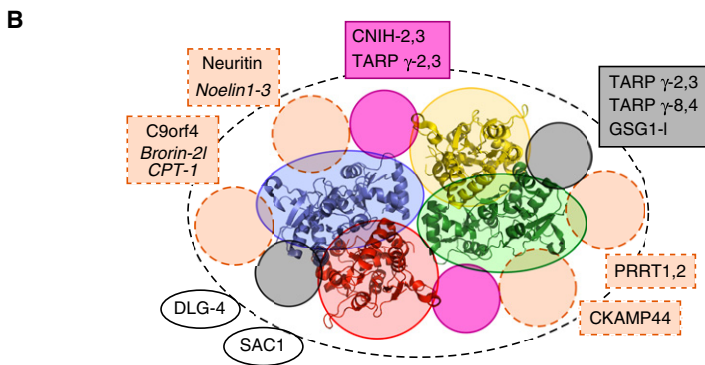
A

B
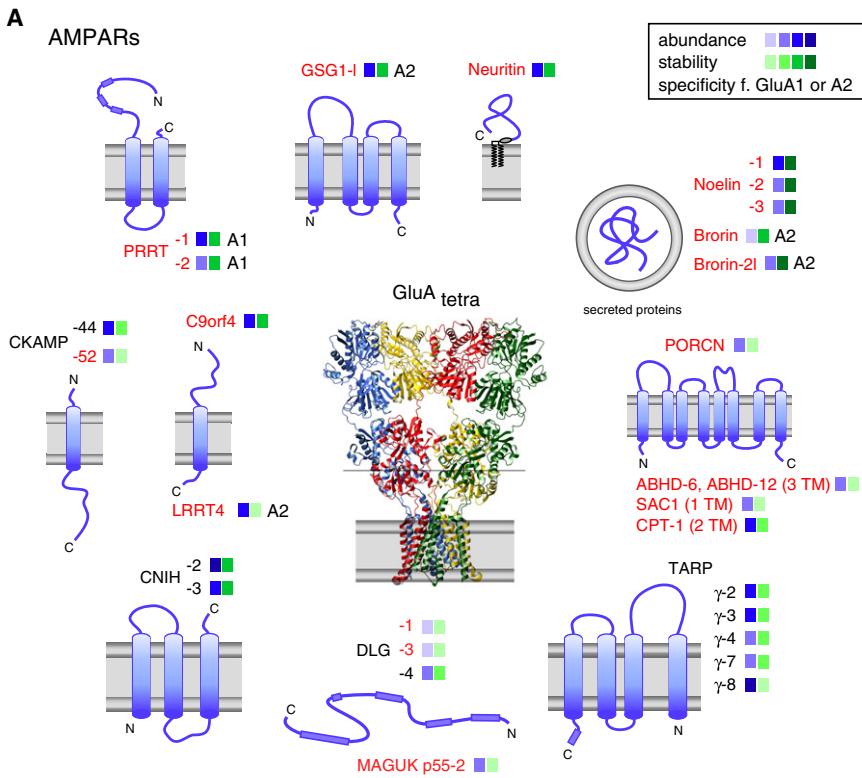
Figure 6. Assembly of Native AMPARs as Determined by Topology and Binding Properties of Their Constituents

(A) Topology of all AMPAR constituents (newly identified proteins in red) and characteristics of their integration into AMPAR complexes. Color coding for their abundance and association stability (from left (minimal) to right (maximal) derived from the data in Figures 2 and 4) in the upper-right corner. Specificity denoted for interaction with GluA1 or GluA2 is indicated.

(B) Model for the assembly of native AMPARs as derived from the proteomic (abundance, stoichiometry of CNIHs and TARPs, populations of AMPARs, Figure 2), biochemical (formation of distinct complexes, direct interaction with GluAs, distinct binding characteristics/stabilities of TARPs γ-8 and γ-2,3, Figures 2–4, Figure S6C), and functional analyses (formation of heteromers from CNIH-2 and GSG1-l, Figures 2 and 5) described in the text and the present knowledge from literature/databases. The view of the GluA-tetramer is from a cross-section of the crystal structure (Sobolevsky et al., 2009) above the membrane plane (gray line in A); solid circles in red and gray depict the suggested asymmetric pairs of binding sites for the indicated inner core constituents; dashed circles in orange are suggested binding sites for the indicated outer core components PRRTs, CKAMP44, C9orf4, and Neuritin that interact directly with the GluA proteins (Figure S6C). The Noelins, Brorin-2l, and CPT-1 are boxed with Neuritin and C9orf4 with which they were found tightly correlated (Pearson correlation analyses, Figure S6B). Dashed line in black delineates periphery/entity of the AMPAR complex; open circles indicate constituents without yet defined interaction with the core proteins. AMPAR constituents for which no further information on binding or coassembly is in hand were left out.

multiple populations of AMPARs with different size and molecular composition (Figure 2). In addition, BN-MS was instrumental to monitor the changes in AMPAR composition induced by the distinct stringencies of solubilization buffers (Figures 2 and 4). It is noteworthy that the entire pool of AMPARs was soluble with buffers of mild/intermediate stringency, in line with the significant mobility of AMPARs in the synaptic membrane (Heine et al., 2008), but in marked contrast to NMDA-type glutamate receptors (Figure S2B) or Cav2 channels (Müller et al., 2010) that are both embedded into larger protein networks. Thus, AMPARs are multiprotein complexes of defined size with an architecture characterized by a common core and variable periphery (Figure 6B). This core offers two pairs of asymmetric binding sites that, in the vast majority of AMPARs, are occupied by different types of auxiliary subunits, TARP γ-8 and CNIH-2 being presumably the most abundant combination therein (Figure 2; also Kato et al., 2010). In fact, at one pair of these sites the CNIHs compete with TARPs γ-2,3, in line with a recent

and, importantly, (3) the use of control tissue from AB-target knockout animals. In addition, the consistency criterion guaranteed reliability of the identified AMPAR constituents. The resulting well-defined proteome of the AMPARs from rodent brain covered the previously known pore-forming and auxiliary subunits, and in addition identified 21 proteins as novel constituents of AMPAR complexes (Figure 1). Most of them are secreted or TM proteins of low molecular weight, constraints imposing intrinsic difficulties on their detection and quantification by mass spectrometry.

Subsequent BN-MS analysis provided data on the relative molecular abundance of individual AMPAR constituents based on protein quantification by calibration peptides (label-free QconCAT technique, Figures 2 and 4) and directly visualized

suggestion (Gill et al., 2011), while the other pair may be occupied by TARPs γ-2,3,4,8 or the structurally related GSG1-l (Figures 6A and 6B). The stability of association observed for the individual components of core and periphery of the AMPAR complexes may be quite distinct (Figure 4). Consequently, comprehensive analysis of the native AMPARs required solubilization with a set of conditions, rather than use of a single buffer system (Nakagawa et al., 2005; Schulte et al., 2011). In addition, it should be noted that the presented AMPAR proteome relies on the sensitivity and dynamic range of our MS analyses. Thus, proteins interacting with the AMPAR complexes at high dynamics or proteins with very low or highly select expression (resulting in protein amounts < 0.1 femtomole) may have escaped detection (Bildl et al., 2012; Müller et al., 2010).

Implications for AMPAR Physiology in Excitatory Synaptic Transmission

About half of the newly identified AMPAR constituents lack any annotation of primary function(s) in public databases and scientific literature, while others have not yet been investigated for their role in AMPAR function. Thus, the results obtained with the not yet annotated GSG1-l protein are significant in two aspects: first, they assign GSG1-l the role of an inner core constituent modifying the gating of AMPARs similar to the other known auxiliary subunits (Figures 2–5). Second, they demonstrate the distinct functional consequences generated by coassembly of different types of auxiliary subunits into the same AMPAR (Figure 5). This observation emphasizes the general importance of heteromultimeric assemblies, as observed with most AMPARs in the brain (Figures 2 and 3), and indicates that AMPAR functions beyond ligand-driven channel gating may be largely determined by their non-GluA constituents.

For a few of the AMPAR constituents identified here, databases and literature offer some striking links toward AMPAR function and physiology. Thus, the membrane-anchored Neuritin, originally identified as *cpg15* in a screen for plasticity-related genes in the hippocampus (Nedivi et al., 1993), was shown to promote maturation of synapses supposedly by recruiting AMPARs to the postsynapse (Cantallops et al., 2000). Similar roles may be expected for LRRT4, a member of the LRRTM family of proteins recently shown to promote formation of excitatory synapses (Ko et al., 2009; Linhoff et al., 2009), or for PRRTs 1,2 that are structurally related to SynDIG1, a protein involved in the development of excitatory synapses (Kalashnikova et al., 2010). Finally, CPT-1 and PORCN are TM proteins with enzymatic activities involved in palmitoylation of cysteine residues, a posttranslational modification that was shown to occur on all GluAs and to modulate receptor trafficking (Hayashi et al., 2005); similarly, modulation of AMPAR trafficking related to synaptic plasticity has been reported for the small GTP-binding protein Rap-2b (Hussain et al., 2010; Zhu et al., 2002).

In conclusion, the AMPAR proteome as presented here defines the molecular framework for the complex cell physiology of AMPARs in excitatory synaptic transmission and provides a roadmap for further in-depth structural and functional investigations.

EXPERIMENTAL PROCEDURES

Molecular Biology

Preparation and injection of cRNAs into *Xenopus* oocytes were done as described (Fakler et al., 1995). All cDNAs were verified by sequencing; GenBank accession numbers of the clones used are as follows: M38060.1 (GluA1$_i$, flip variant of GluA1), NM_017261.2 (GluA2$_i$), NM_053351 (TARP γ-2), NM_001025132 (CNIH-2), NM_080696.2 (TARP γ-8), XM_574558.2 (GSG1-l), NM_014334.2 (C9orf4), NM_053346.1 (Neuritin), NM_001174086.1 (CKAMP44), and NM_001032285.1 (PRRT1). Characterization of AB-specific immunoreactivity (Figure S5) was done as described in (Schwenk et al., 2009).

Biochemistry
Membrane Protein Solubilization

Plasma membrane-enriched protein fractions were prepared from brains (Berkefeld et al., 2006) of adult rat and mice (pooled from more than 20 WT and one to four knockout animals, respectively). Membrane proteins were solubilized for 30 min at 4°C with one of the following buffers (at 1 mg protein / ml): CL-47, CL-48, CL-91, CL-114 (Logopharm GmbH), Triton-buffer (50 mM Tris/HCl pH 8.0 / 150 mM NaCl / 1% Triton X-100), or RIPA-buffer (50 mM Tris/HCl pH 7.4 / 150 mM NaCl / 1% NP40 / 0.5% Deoxycholate / 0.1% SDS); each buffer was supplemented with freshly added protease inhibitors. Nonsolubilized material was subsequently removed by ultracentrifugation (10 min at 150,000 × *g*). The efficiency of solubilization was controlled by western blot analysis of SDS-PAGE resolved aliquots of the soluble fraction (supernatant) and the pellets.

Analytical BN-PAGE

Two-dimensional BN-PAGE/SDS-PAGE separations were essentially done as described (Schwenk et al., 2009). Protein complexes were solubilized in CL-47, CL-48, or CL-91 and centrifuged on a sucrose gradient (400,000 × *g*, 60 min) to replace salt by 0.5 M betaine. For AB-shift experiments the solubilisates were preincubated with the respective ABs for 30 min on ice. After addition of 0.05% Coomassie G250 the samples were separated on linear 3%–8% or 3%–15% polyacrylamide gradient gels in 15 mM BisTris / 50 mM Tricine / 0.01% Coomassie G250 running buffer and 15 mM BisTris (pH 7.0) as anode buffer. A mixture of native proteins (GE Healthcare, USA) and rat mitochondrial membrane protein complexes (Wittig et al., 2010) were run as a standard for complex size in the first dimension. Excised BN-PAGE lanes were incubated for 15 min in Laemmli buffer and placed on top of 10% or 15% SDS-PAGE gels. After electroblotting on PVDF membranes the blot was cut horizontally into different molecular weight ranges and stained with the indicated ABs.

Preparative BN-PAGE

For BN-MS analysis, protein complexes were solubilized from 3 mg (CL-47) or 1 mg (CL-48) rat brain membranes and prepared as detailed above. Samples were resolved on linear 1%–11% polyacrylamide gels (2.5 cm lanes) using the described BN-PAGE buffer system, and the respective gel lanes were collected and frozen at −20°C. The section of interest (~3 × 2 cm) was trimmed, frozen, and sliced in 0.4 mm sections on a cryomicrotome (Leica CM 1950). Slices were thoroughly washed with fixative (30% ethanol / 15% acetic acid) and subjected to in-gel tryptic digestion (81 slices for CL-47 and 69 slices for CL-48 separations).

Affinity Purifications

Solubilisates (1.5 ml) were directly incubated with 10 μg immobilized ABs at 4°C for 2 hr. The following ABs were used for affinity purifications: *anti-GluA1-a* (Millipore, #AB1504), *anti-GluA1-b* (Synaptic System, #182-003), *anti-GluA1-c* (Synaptic System, #182-011), *anti-GluA2-a* (Millipore, #AB1768), *anti-GluA2-b* (NeuroMab, #75-002), *anti-GluA2-c* (Santa Cruz, #sc7610), *anti-GluA2/3* (Millipore, #07-598), *anti-GluA3* (Synaptic System, #182-203), *anti-GluA4-a* (Millipore, #AB1508), *anti-GluA4-b* (Santa Cruz, #sc-7614), *anti-CNIH-2/3* (Hoshino et al., 2007), *anti-TARP γ-8* (Frontier Institute, RB Af1000-1), *anti-TARP γ-2* (Upstate, #07-577), *anti-CKAMP44* (kind gift of Dr. R. Sprengel, von Engelhardt et al., 2010), *anti-GSG1-like* (raised in rabbit against aa 257-278 of Swiss-Prot accession Q6UXU4, affinity purified), *anti-PRRT1* (raised in rabbit against aa 36-54 of Swiss-Prot accession Q6MG82, affinity purified), *anti-Noelin1* (R&D Systems, #AF4636), and *anti-FLAG* (Sigma, #F3165). After brief washing with the respective detergent buffer bound

proteins were eluted with Laemmli buffer (DTT added after elution). Isolated proteins were shortly run into SDS-PAGE gels, silver stained, cut in two pieces of MW > 50 and MW < 50 kDa, and in-gel digested with trypsin (Pandey and Mann, 2000).

Western analyses were performed with *anti-GluA1-a*, *anti-GluA2* (Millipore, MAB397), *anti-GluA2/3*, *anti-GluA3*, *anti-GluA4-a*, *anti-TARP γ-2*, *anti-TARP γ-8*, *anti-CKAMP44*, *anti-GSG1-like* (Sigma, #HPA014479), and *anti-CNIH-2/3* ABs. The AB-stained bands were visualized by *anti-mouse*, *-rabbit*, *-goat IgG*-HRP (all Santa Cruz), and ECL+ (GE Healthcare).

QconCAT Calibration Standard
Two to six consistent peptides specific for each of the identified AMPAR constituents (Table S4) as well as three control proteins were selected and randomly fused in silico to form three N- and C-terminally tagged standard (QconCAT) proteins (84, 60, and 82 peptides resulting in QconCAT proteins of 907 aa, 743 aa, and 942 aa, respectively). The corresponding gene sequences were synthesized (GenScript) and subcloned in a modified pET16 vector; calibration proteins were expressed in *Escherichia coli* BL21(DE3). After verification of full-length expression by dual western blots using *anti-tag* ABs, two-fold dilutions of the QconCAT proteins (seven to nine steps) were separated by SDS-PAGE. The corresponding protein bands were visualized by Coomassie staining, excised, and separately digested by trypsin for subsequent triplicate mass spectrometric analysis.

Mass Spectrometry
LC-MS/MS Analysis
Extracted postdigest peptide mixtures dissolved in 0.5% (v/v) trifluoroacetic acid were analyzed by nano-LC-MS/MS with a LTQ FT Ultra mass spectrometer as described (Müller et al., 2010). Precursor signals were acquired with a target value of 1,000,000 and a nominal resolution of 100,000 (FWHM) at m/z 400 (scan range 370 to 1700 m/z). Up to five data-dependent CID fragment spectra per scan cycle were acquired in the ion trap with a target value of 10,000 (maximum injection time 400 ms) with dynamic exclusion enabled. Total MS acquisition times were 105 min (75 min rising acetonitrile concentration, 30 s dynamic MS/MS exclusion) for AP eluate fractions and 170 min (140 min rising acetonitrile concentration, 60 s dynamic MS/MS exclusion) for BN-PAGE fractions, respectively.

Database Search
LC-MS/MS data was extracted using the extract_msn utility and searched against the UniProt Knowledgebase release 2010_11 using the Mascot search engine (version 2.3.01; Matrix Science) with tolerance for peptide mass and fragment mass set to 15 ppm and 0.8 ppm, respectively. One missed trypsin cleavage and common variable modifications were accepted for peptide identification. After linear shift mass recalibration the peptide mass window was narrowed to ± 5 ppm for final searches. The final search database contained all UniProtKB/Swiss-Prot entries for *Mus musculus*, *Rattus norvegicus*, and *Homo sapiens* including P00761, P00766, P02769, P11886, and P41921 as well as 22 UniProtKB/TrEMBL homologs to previously (in the course of this study) identified AMPAR complex constituents of these species. Proteins identified by only one specific MS/MS spectrum were not further considered. The average effective peptide FDR for all evaluated proteins (calculated as the number of corresponding peptides identified with a Mascot ion score ≥ 20 for the real database versus respective hits in a decoy database) was 0.029 (SD 0.021).

Relative Amino Acid Sequence Coverage
Relative amino acid sequence coverage of proteins (Figures 1D and Table S2) was calculated as $SC = N_i / (N_i + N_{an})$, where N_i is the number of amino acid residues covered by identified peptides (Mascot e-value < 0.05, retrieval in > 2 independent APs) and N_{an} is the number of MS-accessible (peptides within 740 < MW < 3,000 with trypsin cleavage C-terminal to the basic amino acids, but not N-terminal to proline; missed cleavages were not considered) but not identified amino acids in the respective database sequence.

Protein Quantification Procedures
For peak volume-based quantification, m/z features along LC-MS scans were detected and quantified (as intensity × retention time × m/z width) using msInspect (Computational Proteomics Laboratory, Fred Hutchinson Cancer Research Center, Seattle, WA, USA). After correction of m/z shifts (based on MS-sequenced peptides using an in-house written script), features were aligned between different LC-MS/MS runs and assigned to the peptides identified by Mascot (retention time tolerance: 3% or 1 min, m/z difference threshold: ± 5 ppm). The resulting peptide peak volumes (PVs) were used for two different quantification procedures.

Protein Abundance Ratios (rPV). In AP versus control (Figure 1), these were determined using the TopCorr method detailed in (Bildl et al., 2012; Supplemental Experimental Procedures). Protein rPV values were plotted for each AB (AP versus controls, e.g., Figure 1B) to derive specificity thresholds from the resulting ratio distributions. Proteins were considered specifically copurified when rPV(versus IgG) > threshold(IgG) in both rat and mouse, and no cross-reactivity was indicated by rPV(versus KO) < threshold(versus KO) (Figure 1).

Relative Molar Abundances of Proteins. In a sample (Figures 2 and 4), these were determined as follows: dilution series of the QconCAT proteins (total of 171 peptides, see above) were measured by LC-MS/MS three times and the extracted peptide PVs checked for reproducibility and linearity over at least two orders of magnitude. For each peptide slope factors were determined by linear regression fits to the measured PVs versus dilution factor of the load reflecting each peptide's specific MS signal intensity (Figure S2; loads of the three concatenated standards were normalized to each other by their abundance_norm values; Zolles et al., 2009). These slope factors were then used to normalize the respective peptide PVs in APs or BN-PAGE slices to an equimolar basis. The relative molar abundance of each protein was then calculated as intensity-weighted mean (AP data sets) or median (BN-PAGE samples) of the respective normalized peptide PVs. To establish *protein profiles* across BN-PAGE samples (Figure 2), the respective PV tables were preprocessed: (1) each individual slice measurement (i.e., LC-MS data set) was scaled by dividing its average PV to a sliding average PV of the neighboring two slices (window of 5) to account for variations in slice thickness, peptide recovery and LC-MS sensitivity and (2) a filter was applied to eliminate false-positive PV assignments (identified as solitary values without backup from the neighboring two slices or > 10-fold outliers with respect to the average of corresponding PVs in the neighboring two slices) and to bridge gaps resulting from false-negative assignments (individual missing values were replaced by the corresponding PV average of the neighboring slices, if available). The resulting relative molar protein abundances were finally smoothened by averaging (window of 3).

Electron Microscopy
Hippocampal sections of adult Wistar rats (CA3 area, 80 nm thick) were processed for the postembedding immunogold labeling as described earlier (Kulik et al., 2002; Schwenk et al., 2009) and stained with affinity-purified mouse *anti-GluA2/4* (*Millipore*, #MAB396) and two different rabbit *anti-GSG1-l* ABs (raised against aa 83-102 and aa 257-278; Figure S5B). Secondary ABs (1:20; British Biocell International, Cardiff, UK) were coupled to either 10 nm gold particles (for GluR2/4) or 15 nm gold particles (for GSG1-l).

Electrophysiological Recordings and Data Analysis
Electrophysiological recordings from giant outside-out patches excised from oocytes were performed at room temperature (22°C –24°C) as described previously (Berkefeld et al., 2006). Currents were recorded with an EPC9 amplifier, low-pass filtered at 3 kHz and sampled at 5–10 kHz. Pipettes made from thick-walled borosilicate glass had resistances of 0.4–0.8 MΩ when filled with intracellular solution (K_{int}; in mM) 120 KCl, 5 HEPES, 10 EGTA, pH adjusted to 7.2. Extracellular solution (K_{ext}) applied to outside-out patches was composed as follows (mM): 120 KCl, 5 HEPES, 1.3 CaCl₂ (pH 7.2). Rapid application/removal of glutamate (1 mM, dissolved in K_{ex}) was performed using a Piezo-controlled fast application system with a double-barrel application pipette that enables solution exchanges within less than 100 μs (20%–80%), measured from the open tip response during a switch between normal and 10×-diluted K_{ext}.

Deactivation, desensitization, and recovery from desensitization of AMPARs were characterized by time constants derived from monoexponential fits to the decay phase or recovery of the glutamate-activated currents; the quality of the fit result was judged from the sum of squared differences value. Curve fitting and further data analysis were done with Igor Pro 4.05A Carbon. Data in text and figures are given as mean ± SD, unless specified differently.

REFERENCES

Bats, C., Groc, L., and Choquet, D. (2007). The interaction between Stargazin and PSD-95 regulates AMPA receptor surface trafficking. Neuron 53, 719–734.

Berkefeld, H., Sailer, C.A., Bildl, W., Rohde, V., Thumfart, J.O., Eble, S., Klugbauer, N., Reisinger, E., Bischofberger, J., Oliver, D., et al. (2006). BKCa-Cav channel complexes mediate rapid and localized Ca^{2+}-activated K^+ signaling. Science 314, 615–620.

Bildl, W., Haupt, A., Muller, C.S., Biniossek, M., Thumfart, J.O., Hüber, B., Fakler, B., and Schulte, U. (2012). Extending the dynamic range of label-free mass spectrometric quantification of affinity purifications. Mol. Cell. Proteomics. 11, M111.007955.

Bredt, D.S., and Nicoll, R.A. (2003). AMPA receptor trafficking at excitatory synapses. Neuron 40, 361–379.

Cantallops, I., Haas, K., and Cline, H.T. (2000). Postsynaptic CPG15 promotes synaptic maturation and presynaptic axon arbor elaboration in vivo. Nat. Neurosci. 3, 1004–1011.

Carroll, R.C., Beattie, E.C., von Zastrow, M., and Malenka, R.C. (2001). Role of AMPA receptor endocytosis in synaptic plasticity. Nat. Rev. Neurosci. 2, 315–324.

Chen, L., Chetkovich, D.M., Petralia, R.S., Sweeney, N.T., Kawasaki, Y., Wenthold, R.J., Bredt, D.S., and Nicoll, R.A. (2000). Stargazin regulates synaptic targeting of AMPA receptors by two distinct mechanisms. Nature 408, 936–943.

Cho, C.H., St-Gelais, F., Zhang, W., Tomita, S., and Howe, J.R. (2007). Two families of TARP isoforms that have distinct effects on the kinetic properties of AMPA receptors and synaptic currents. Neuron 55, 890–904.

Choquet, D. (2010). Fast AMPAR trafficking for a high-frequency synaptic transmission. Eur. J. Neurosci. 32, 250–260.

Choquet, D., and Triller, A. (2003). The role of receptor diffusion in the organization of the postsynaptic membrane. Nat. Rev. Neurosci. 4, 251–265.

Collingridge, G.L., Olsen, R.W., Peters, J., and Spedding, M. (2009). A nomenclature for ligand-gated ion channels. Neuropharmacology 56, 2–5.

Conti, F., and Weinberg, R.J. (1999). Shaping excitation at glutamatergic synapses. Trends Neurosci. 22, 451–458.

Cull-Candy, S., Kelly, L., and Farrant, M. (2006). Regulation of Ca^{2+}-permeable AMPA receptors: synaptic plasticity and beyond. Curr. Opin. Neurobiol. 16, 288–297.

Derkach, V.A., Oh, M.C., Guire, E.S., and Soderling, T.R. (2007). Regulatory mechanisms of AMPA receptors in synaptic plasticity. Nat. Rev. Neurosci. 8, 101–113.

Fakler, B., Brändle, U., Glowatzki, E., Weidemann, S., Zenner, H.P., and Ruppersberg, J.P. (1995). Strong voltage-dependent inward rectification of inward rectifier K^+ channels is caused by intracellular spermine. Cell 80, 149–154.

Garaschuk, O., Schneggenburger, R., Schirra, C., Tempia, F., and Konnerth, A. (1996). Fractional Ca^{2+} currents through somatic and dendritic glutamate receptor channels of rat hippocampal CA1 pyramidal neurones. J. Physiol. 491, 757–772.

Gill, M.B., Kato, A.S., Roberts, M.F., Yu, H., Wang, H., Tomita, S., and Bredt, D.S. (2011). Cornichon-2 modulates AMPA receptor-transmembrane AMPA receptor regulatory protein assembly to dictate gating and pharmacology. J. Neurosci. 31, 6928–6938.

Harmel, N., Cokic, B., Zolles, G., Berkefeld, H., Mauric, V., Fakler, B., Stein, V., and Klöcker, N. (2012). AMPA receptors commandeer an ancient cargo exporter for use as an auxiliary subunit for signaling. PLoS ONE 7, e30681.

Hayashi, T., Rumbaugh, G., and Huganir, R.L. (2005). Differential regulation of AMPA receptor subunit trafficking by palmitoylation of two distinct sites. Neuron 47, 709–723.

Heine, M., Groc, L., Frischknecht, R., Béïque, J.C., Lounis, B., Rumbaugh, G., Huganir, R.L., Cognet, L., and Choquet, D. (2008). Surface mobility of postsynaptic AMPARs tunes synaptic transmission. Science 320, 201–205.

Hollmann, M., and Heinemann, S. (1994). Cloned glutamate receptors. Annu. Rev. Neurosci. 17, 31–108.

Hoshino, H., Uchida, T., Otsuki, T., Kawamoto, S., Okubo, K., Takeichi, M., and Chisaka, O. (2007). Cornichon-like protein facilitates secretion of HB-EGF and regulates proper development of cranial nerves. Mol. Biol. Cell 18, 1143–1152.

Hussain, N.K., Hsin, H., Huganir, R.L., and Sheng, M. (2010). MINK and TNIK differentially act on Rap2-mediated signal transduction to regulate neuronal structure and AMPA receptor function. J. Neurosci. 30, 14786–14794.

Jonas, P. (2000). The Time Course of Signaling at Central Glutamatergic Synapses. News Physiol. Sci. 15, 83–89.

Jonas, P., and Spruston, N. (1994). Mechanisms shaping glutamate-mediated excitatory postsynaptic currents in the CNS. Curr. Opin. Neurobiol. 4, 366–372.

Kalashnikova, E., Lorca, R.A., Kaur, I., Barisone, G.A., Li, B., Ishimaru, T., Trimmer, J.S., Mohapatra, D.P., and Díaz, E. (2010). SynDIG1: an activity-regulated, AMPA- receptor-interacting transmembrane protein that regulates excitatory synapse development. Neuron 65, 80–93.

Kato, A.S., Gill, M.B., Ho, M.T., Yu, H., Tu, Y., Siuda, E.R., Wang, H., Qian, Y.W., Nisenbaum, E.S., Tomita, S., and Bredt, D.S. (2010). Hippocampal AMPA receptor gating controlled by both TARP and cornichon proteins. Neuron 68, 1082–1096.

Kim, K.S., Yan, D., and Tomita, S. (2010). Assembly and stoichiometry of the AMPA receptor and transmembrane AMPA receptor regulatory protein complex. J. Neurosci. 30, 1064–1072.

Ko, J., Fuccillo, M.V., Malenka, R.C., and Südhof, T.C. (2009). LRRTM2 functions as a neurexin ligand in promoting excitatory synapse formation. Neuron 64, 791–798.

Kulik, A., Nakadate, K., Nyíri, G., Notomi, T., Malitschek, B., Bettler, B., and Shigemoto, R. (2002). Distinct localization of GABA(B) receptors relative to synaptic sites in the rat cerebellum and ventrobasal thalamus. Eur. J. Neurosci. 15, 291–307.

Linhoff, M.W., Laurén, J., Cassidy, R.M., Dobie, F.A., Takahashi, H., Nygaard, H.B., Airaksinen, M.S., Strittmatter, S.M., and Craig, A.M. (2009). An unbiased expression screen for synaptogenic proteins identifies the LRRTM protein family as synaptic organizers. Neuron 61, 734–749.

Malenka, R.C., and Nicoll, R.A. (1999). Long-term potentiation—a decade of progress? Science 285, 1870–1874.

Malinow, R., and Malenka, R.C. (2002). AMPA receptor trafficking and synaptic plasticity. Annu. Rev. Neurosci. 25, 103–126.

McAllister, A.K. (2007). Dynamic aspects of CNS synapse formation. Annu. Rev. Neurosci. 30, 425–450.

McKinney, R.A. (2010). Excitatory amino acid involvement in dendritic spine formation, maintenance and remodelling. J. Physiol. 588, 107–116.

Milstein, A.D., Zhou, W., Karimzadegan, S., Bredt, D.S., and Nicoll, R.A. (2007). TARP subtypes differentially and dose-dependently control synaptic AMPA receptor gating. Neuron 55, 905–918.

Müller, C.S., Haupt, A., Bildl, W., Schindler, J., Knaus, H.G., Meissner, M., Rammner, B., Striessnig, J., Flockerzi, V., Fakler, B., and Schulte, U. (2010). Quantitative proteomics of the Cav2 channel nano-environments in the mammalian brain. Proc. Natl. Acad. Sci. USA *107*, 14950–14957.

Nakagawa, T., Cheng, Y., Ramm, E., Sheng, M., and Walz, T. (2005). Structure and different conformational states of native AMPA receptor complexes. Nature *433*, 545–549.

Nedivi, E., Hevroni, D., Naot, D., Israeli, D., and Citri, Y. (1993). Numerous candidate plasticity-related genes revealed by differential cDNA cloning. Nature *363*, 718–722.

Newpher, T.M., and Ehlers, M.D. (2008). Glutamate receptor dynamics in dendritic microdomains. Neuron *58*, 472–497.

Pandey, A., and Mann, M. (2000). Proteomics to study genes and genomes. Nature *405*, 837–846.

Pratt, J.M., Simpson, D.M., Doherty, M.K., Rivers, J., Gaskell, S.J., and Beynon, R.J. (2006). Multiplexed absolute quantification for proteomics using concatenated signature peptides encoded by QconCAT genes. Nat. Protoc. *1*, 1029–1043.

Raman, I.M., and Trussell, L.O. (1992). The kinetics of the response to glutamate and kainate in neurons of the avian cochlear nucleus. Neuron *9*, 173–186.

Remmerie, N., De Vijlder, T., Valkenborg, D., Laukens, K., Smets, K., Vreeken, J., Mertens, I., Carpentier, S.C., Panis, B., De Jaeger, G., et al. (2011). Unraveling tobacco BY-2 protein complexes with BN PAGE/LC-MS/MS and clustering methods. J. Proteomics *74*, 1201–1217.

Sah, P., Hestrin, S., and Nicoll, R.A. (1990). Properties of excitatory postsynaptic currents recorded in vitro from rat hippocampal interneurones. J. Physiol. *430*, 605–616.

Schober, D.A., Gill, M.B., Yu, H., Gernert, D.L., Jeffries, M.W., Ornstein, P.L., Kato, A.S., Felder, C.C., and Bredt, D.S. (2011). Transmembrane AMPA receptor regulatory proteins and cornichon-2 allosterically regulate AMPA receptor antagonists and potentiators. J. Biol. Chem. *286*, 13134–13142.

Schulte, U., Müller, C.S., and Fakler, B. (2011). Ion channels and their molecular environments—glimpses and insights from functional proteomics. Semin. Cell Dev. Biol. *22*, 132–144.

Schwenk, J., Harmel, N., Zolles, G., Bildl, W., Kulik, A., Heimrich, B., Chisaka, O., Jonas, P., Schulte, U., Fakler, B., and Klöcker, N. (2009). Functional proteomics identify cornichon proteins as auxiliary subunits of AMPA receptors. Science *323*, 1313–1319.

Schwenk, J., Metz, M., Zolles, G., Turecek, R., Fritzius, T., Bildl, W., Tarusawa, E., Kulik, A., Unger, A., Ivankova, K., et al. (2010). Native GABA(B) receptors are heteromultimers with a family of auxiliary subunits. Nature *465*, 231–235.

Seeburg, P.H. (1993). The TINS/TiPS Lecture. The molecular biology of mammalian glutamate receptor channels. Trends Neurosci. *16*, 359–365.

Shepherd, J.D., and Huganir, R.L. (2007). The cell biology of synaptic plasticity: AMPA receptor trafficking. Annu. Rev. Cell Dev. Biol. *23*, 613–643.

Shi, Y., Lu, W., Milstein, A.D., and Nicoll, R.A. (2009). The stoichiometry of AMPA receptors and TARPs varies by neuronal cell type. Neuron *62*, 633–640.

Shi, Y., Suh, Y.H., Milstein, A.D., Isozaki, K., Schmid, S.M., Roche, K.W., and Nicoll, R.A. (2010). Functional comparison of the effects of TARPs and cornichons on AMPA receptor trafficking and gating. Proc. Natl. Acad. Sci. USA *107*, 16315–16319.

Silver, R.A., Traynelis, S.F., and Cull-Candy, S.G. (1992). Rapid-time-course miniature and evoked excitatory currents at cerebellar synapses in situ. Nature *355*, 163–166.

Sobolevsky, A.I., Rosconi, M.P., and Gouaux, E. (2009). X-ray structure, symmetry and mechanism of an AMPA-subtype glutamate receptor. Nature *462*, 745–756.

Soto, D., Coombs, I.D., Kelly, L., Farrant, M., and Cull-Candy, S.G. (2007). Stargazin attenuates intracellular polyamine block of calcium-permeable AMPA receptors. Nat. Neurosci. *10*, 1260–1267.

Soto, D., Coombs, I.D., Renzi, M., Zonouzi, M., Farrant, M., and Cull-Candy, S.G. (2009). Selective regulation of long-form calcium-permeable AMPA receptors by an atypical TARP, gamma-5. Nat. Neurosci. *12*, 277–285.

Tomita, S., Chen, L., Kawasaki, Y., Petralia, R.S., Wenthold, R.J., Nicoll, R.A., and Bredt, D.S. (2003). Functional studies and distribution define a family of transmembrane AMPA receptor regulatory proteins. J. Cell Biol. *161*, 805–816.

Tomita, S., Adesnik, H., Sekiguchi, M., Zhang, W., Wada, K., Howe, J.R., Nicoll, R.A., and Bredt, D.S. (2005). Stargazin modulates AMPA receptor gating and trafficking by distinct domains. Nature *435*, 1052–1058.

Vandenberghe, W., Nicoll, R.A., and Bredt, D.S. (2005). Stargazin is an AMPA receptor auxiliary subunit. Proc. Natl. Acad. Sci. USA *102*, 485–490.

von Engelhardt, J., Mack, V., Sprengel, R., Kavenstock, N., Li, K.W., Stern-Bach, Y., Smit, A.B., Seeburg, P.H., and Monyer, H. (2010). CKAMP44: a brain-specific protein attenuating short-term synaptic plasticity in the dentate gyrus. Science *327*, 1518–1522.

Wessels, H.J., Vogel, R.O., van den Heuvel, L., Smeitink, J.A., Rodenburg, R.J., Nijtmans, L.G., and Farhoud, M.H. (2009). LC-MS/MS as an alternative for SDS-PAGE in blue native analysis of protein complexes. Proteomics *9*, 4221–4228.

Wittig, I., Beckhaus, T., Wumaier, Z., Karas, M., and Schägger, H. (2010). Mass estimation of native proteins by blue native electrophoresis: principles and practical hints. Mol. Cell. Proteomics *9*, 2149–2161.

Zhu, J.J., Qin, Y., Zhao, M., Van Aelst, L., and Malinow, R. (2002). Ras and Rap control AMPA receptor trafficking during synaptic plasticity. Cell *110*, 443–455.

Zolles, G., Wenzel, D., Bildl, W., Schulte, U., Hofmann, A., Müller, C.S., Thumfart, J.O., Vlachos, A., Deller, T., Pfeifer, A., et al. (2009). Association with the auxiliary subunit PEX5R/Trip8b controls responsiveness of HCN channels to cAMP and adrenergic stimulation. Neuron *62*, 814–825.